since 1961

Baltica

*BALTICA Volume 37 Number 2 December 2024: 151–169*
https://doi.org/10.5200/baltica.2024.2.6

# Artificial neural networks-based ternary charts for predicting strength and frost heaving in mountain soils

***Rustu Orkun Karamut, Adil Binal****

Karamut, R.O., Binal, A. 2024. Artificial neural networks-based ternary charts for predicting strength and frost heaving in mountain soils. *Baltica 37 (2*), 151–169. Vilnius. ISSN 0067-3064.

Manuscript submitted 12 September 2024 / Accepted 21 November 2024 / Available online 9 December 2024



**Abstract.** In recent years, construction has increased at previously uninhabited high altitudes with the development of winter tourism and population growth. Therefore, it is necessary to examine the soil behaviour at low temperatures and high altitudes. This study investigated the physical properties and mechanical behaviours of soil samples collected from four mountainous regions, including settlement areas. In addition, new frost-heaving pressure and strength prediction charts have been developed. Based on sieve analysis, the soil samples from the Kaçkar, Palandöken, Erciyes, and Ilgaz Mountain areas were classified as silty gravel or sand. With increasing elevation, the percentage of coarse particles in soil samples increased, whereas the proportion of fine particles decreased. A new device was developed to investigate the mechanical behaviour of soil samples at low temperatures (0°C and below). The highest frost strength (7274.5 kPa) and heaving pressure (43.97 kPa) were measured in soils with high fine-grain content. A statistical evaluation of the test results was performed, and it was determined that the most influential variables for estimating frost heaving and strength were the fine-grain ratio, soil temperature, and water content. ANN analyses were performed using these variables, and ternary strength and frost-heaving pressure estimation diagrams were developed.

***Keywords:*** *mountain soil; physical-mechanical properties; frost-heaving pressure; ternary diagram*

✉ *Rustu Orkun Karamut (karamut_orkun@hotmail.com)*
*Adil Binal* (adil@hacettepe.edu.tr) https://orcid.org/0000-0002-4183-9430*
*Hacettepe University, Faculty of Engineering, Department of Geological Engineering, Beytepe Campus, 06800, Ankara/Türkiye*
**Corresponding author*

## INTRODUCTION

Periglacial landforms are generally observed around polar circles; however, they can also form in areas with ground temperatures below 0°C at high altitudes, regardless of latitude. The increase in ice volume during freezing and thawing events is the main factor that drives the development of periglacial landforms. In addition to freezing and thawing, intense physical separation and displacement events also occur in these regions (Dede *et al.* 2022). Freeze-thaw (F-T) cycles significantly deteriorate roadbed soil engineering properties and negatively affect road performance and service life in seasonally frozen regions (Sun *et al.* 2021). Additionally, significant frost heave is observed in embankments of high-speed rail (HSR) constructed on seasonally frozen ground, posing a severe threat to railway trains (Wang *et al.* 2021). Understanding the effects of F-T cycles on the physical-mechanical properties of soil is critical for construction stabilisation and damage reduction (Jing *et al.* 2021). Solid mineral particles, air, water, and ice form a frozen-ground system. Ice, which varies significantly in its structure depending on temperature, changes the mechanical properties of frozen ground compared to non-frozen soil (Qi *et al.* 2010). Experimental studies to determine the mechanical properties of frozen soil began at the beginning of the past century (Zhu 1988). Hermansson, Spencer Guthrie (2005) measured freeze-up cycles in clay soil

specimens with different water content from an area in Sweden. The most saturated water samples exhibited the most significant frost-bubble formation. The mechanical properties and microstructures of frozen and thawed soils differ significantly from those of intact soils (Li *et al.* 2021). Wang *et al.* (2007) subjected 22 F-T cycles on Qinghai-Tibetan clay in the temperature range of -7°C to +14°C. After the seventh cycle, the volume of the clay samples increased, water content and cohesion decreased, and the internal friction angle remained unchanged (Oztas, Fayetorbay 2003). The decrease in wet aggregate stability for different particle size groups ranged from 13.8% to 57.7%. Several studies have shown that F-T cycles change the grain size distribution (Adeli Ghareh Viran, Binal 2018; Liu *et al.* 2019a; Wang *et al.* 2020). The shear strength of shallow swelling soil after freeze-thaw cycling significantly differed with depth and was strongly correlated with water content (Liu *et al.* 2019b). Huixin *et al.* (2012) reported that swelling increased with soil density. From an engineering point of view, different project levels require different data precision. For example, a highway requires highly reliable data, whereas a local rural road can be designed using the estimated values. Frost-heave tests produce highly reliable data. However, these tests require sophisticated and costly equipment and are time-consuming, particularly for large samples. The construction and rehabilitation of secondary roads are constrained by financial limitations. Cold-climate regions, such as the Nordic countries and Canada, have large road and railway networks, the majority of which cover long distances in sparsely populated territories (Dore, Zubeck 2009). The frost design of these roads must therefore be optimised considering limited budgets, that is, the frost susceptibility estimation of different soils and geomaterials must be cost-effective and reliable (Loranger *et al.* 2022). The frost susceptibility of a soil type may be evaluated based on the grain size distribution only if the structure in question tolerates frost heave to a certain extent and if the work in question concerns large soil masses. In these cases, classifying soils into frost-susceptible or non-frost-susceptible materials is sufficient, according to the criterion proposed by the International Society for Soil Mechanics and Geotechnical Engineering (ISSMFE) Technical Committee on Frost (1989). If the grain size curve lies completely within the region 1, the soil is always frost-susceptible (FS); in the region 1L, the FS is low. If the grain size curve falls completely inside the regions 2, 3 or 4, the soil is non-FS (Fig. 1) (Slunga, Saarelainen 2005). However, this graph is useless when the groundwater level is close to the surface in glacial valleys because water causing volumetric expansion cannot be filtered through large grains, and soil pore water freezes in place.

The freezing behaviour of soils and granular materials is influenced by many factors, including particle size distribution, mineral composition, water content, density, degree of compaction/consolidation, permeability, capillarity, availability of water, temperature conditions (magnitude, freezing period length, and temperature gradient), and local climate variability. The frost rate was the lowest in the well-graded gravel plots, which were not susceptible to freezing, whereas the frost rate was the highest in the clay and silt soils (Fig. 2) (Konrad 1999; Brandl 2008; Loranger *et al.* 2022).

However, only a few studies have been conducted on the frost susceptibility of soils. These studies generally focused on the frost heave rate. Therefore, in this study, a new device was designed to measure the frost heaving pressure and frost strength of soil. The test results were used to construct ternary plots based on the fine grain content, natural water content, and soil temperature.

## STUDY AREAS

Samples were collected from the Palandöken, Ilgaz, Erciyes, and Kaçkar Mountain areas to determine the physical and mechanical properties of mountain soils in Türkiye. The soil areas and gentle slopes were investigated in this study. Undisturbed and disturbed samples were collected at each sampling site (Fig. 3). Glaciation is limited to the Palandöken Mountains, and there are cirques only on the north-facing slopes of the mountains because of arid climatic and continental conditions (Erinç 1953; Polat 2003). The sampling elevation at Mount Palandöken was 3000 m (Fig. 4a). At Mount Ilgaz, the most common periglacial landform is a non-sorted step, and elevation ranges occur between 1943 m and 2398 m. The organic matter content tended to decrease as elevation increased. A comparable situation was observed in clay formations, although it was not as evident as that in organic matter. For example, the clay contents of the soil at elevations of 1943, 2210, and 2395 m were 33.72%, 27.69%, and 26.62%, respectively (Dede *et al.* 2021). Sampling in this area was performed at a depth of 2000 m (Fig. 4b).

Mount Erciyes, the highest stratovolcano of the Cappadocian Volcanic Province, witnessed widespread valley glaciations during the Late Quaternary. It has four valleys and one ridge, with small glaciers and glacial deposits on its flanks. Aksu Valley is a northwest-trending U-shaped valley with an actual glacier descending to 3400 m in elevation. The lateral and terminal moraines, young ablation moraines, and outwash plains indicate three glacial epochs. The oldest and most extensive type is characterised by two well-preserved, 100 m high lateral moraines at 2200–2900 m (Sarıkaya *et al.* 2003). In the Erciyes

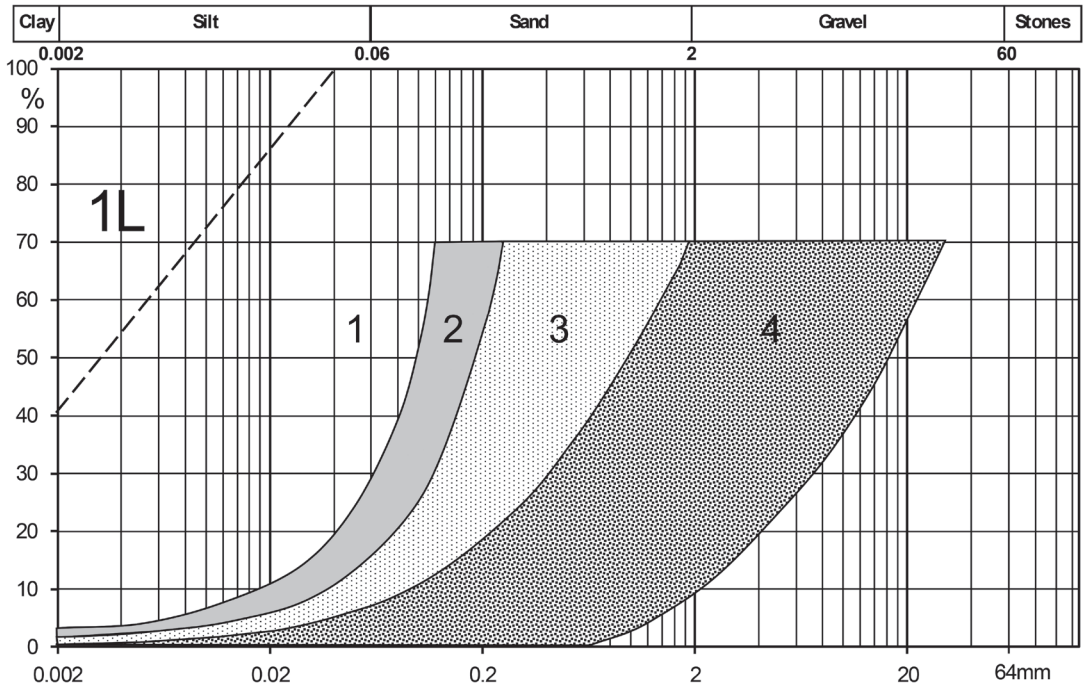


**Fig 1** Determination of the frost susceptibility (FS) of a soil based on a grain size curve (Slunga, Saarelainen 2005)

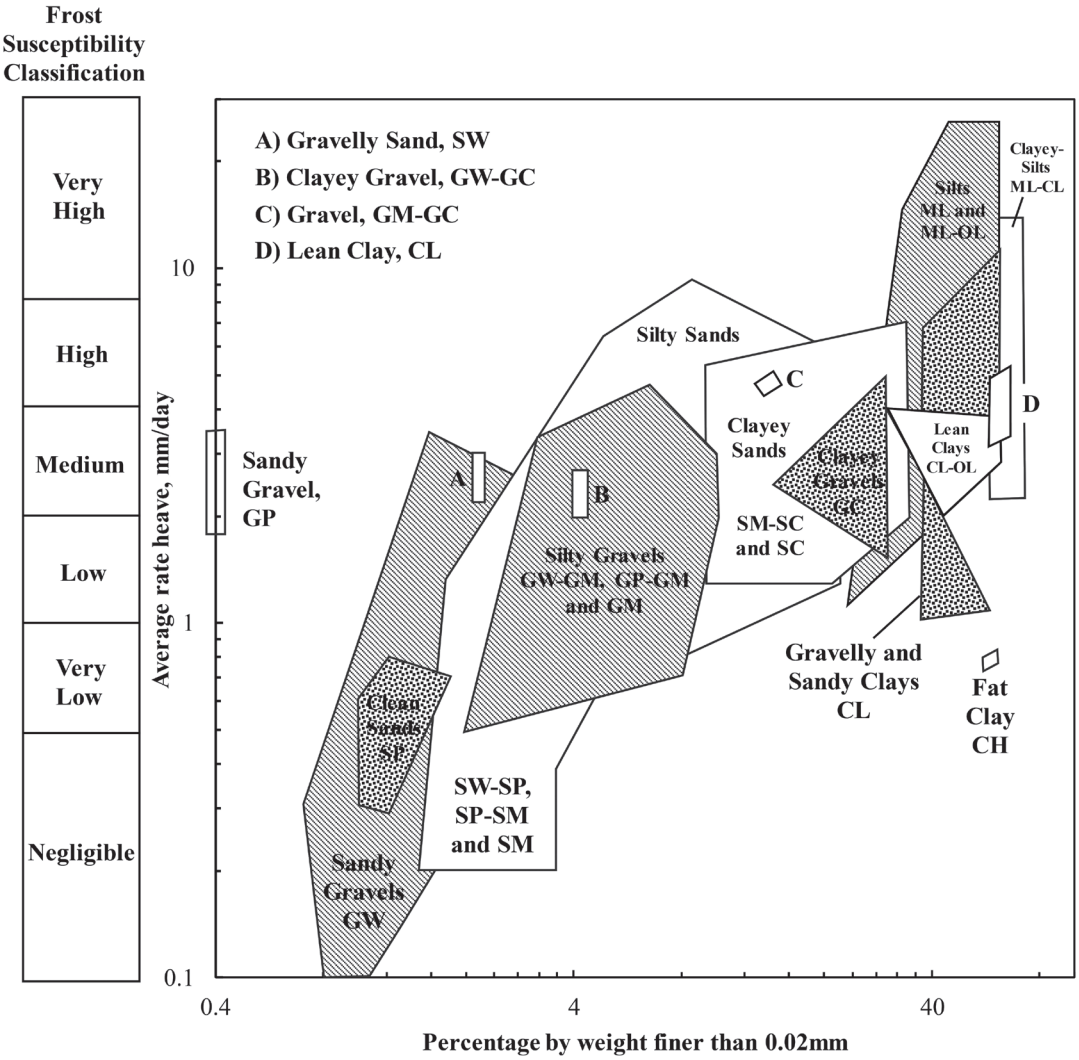


**Fig. 2** Frost heave rates and classification of remoulded soils, U.S. Army Corps of Engineers (Loranger *et al.* 2022)

Mountain (Kayseri) area, pits were opened at a depth of approximately one meter (Fig. 4c) and the temperature change in the pit wall was observed using a thermal camera (Fig. 5a–b). Sampling was performed at altitudes of 2900–3300 m in this locality. Kavron Valley is in the Kackar Mountains in the eastern Black Sea Mountain range of the northeast region of Türkiye. It is a north-south-oriented, typical U-shaped glacial valley that is approximately 12 km long. The mountain range's highest peak rises to 3932 m, with the base of the Kavron Valley falling to approximately 1600 m and consists of one central valley and three tributary valleys (Akçar *et al.* 2007). The Kavron Glacier Valley was selected as the first study area in the Kackar Mountain region. The glacial part of the study area was examined, soil samples were obtained from the Kavron Plateau (Fig. 4d), and imaging was performed using a thermal camera in the excavated

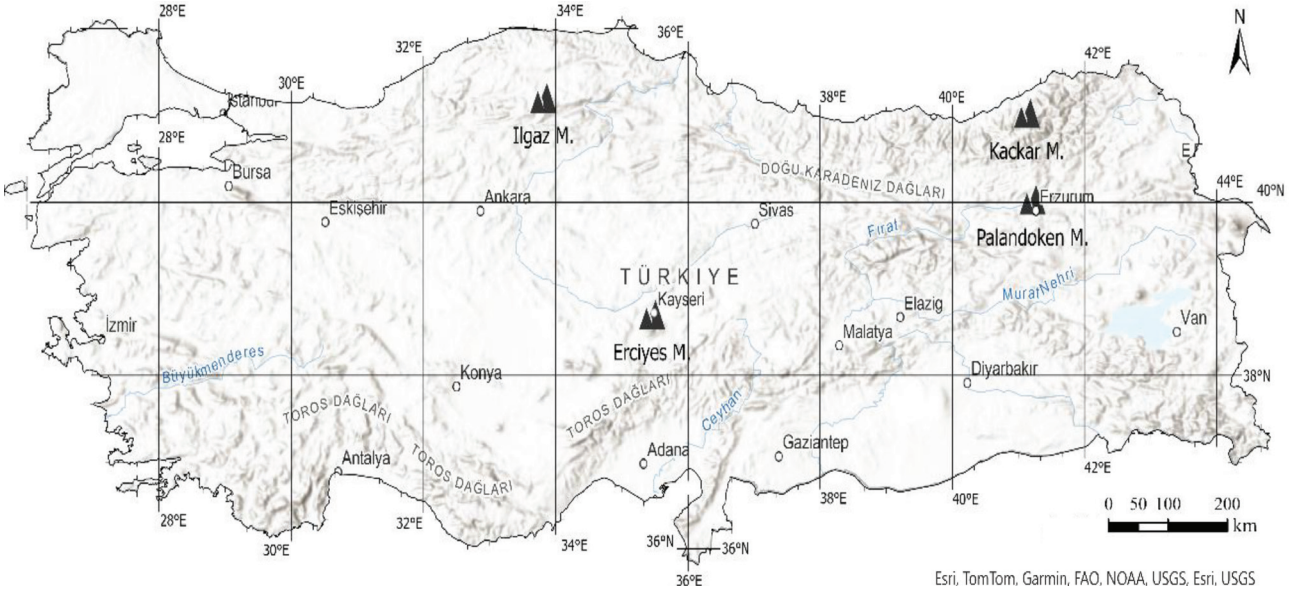


**Fig. 3** Study areas

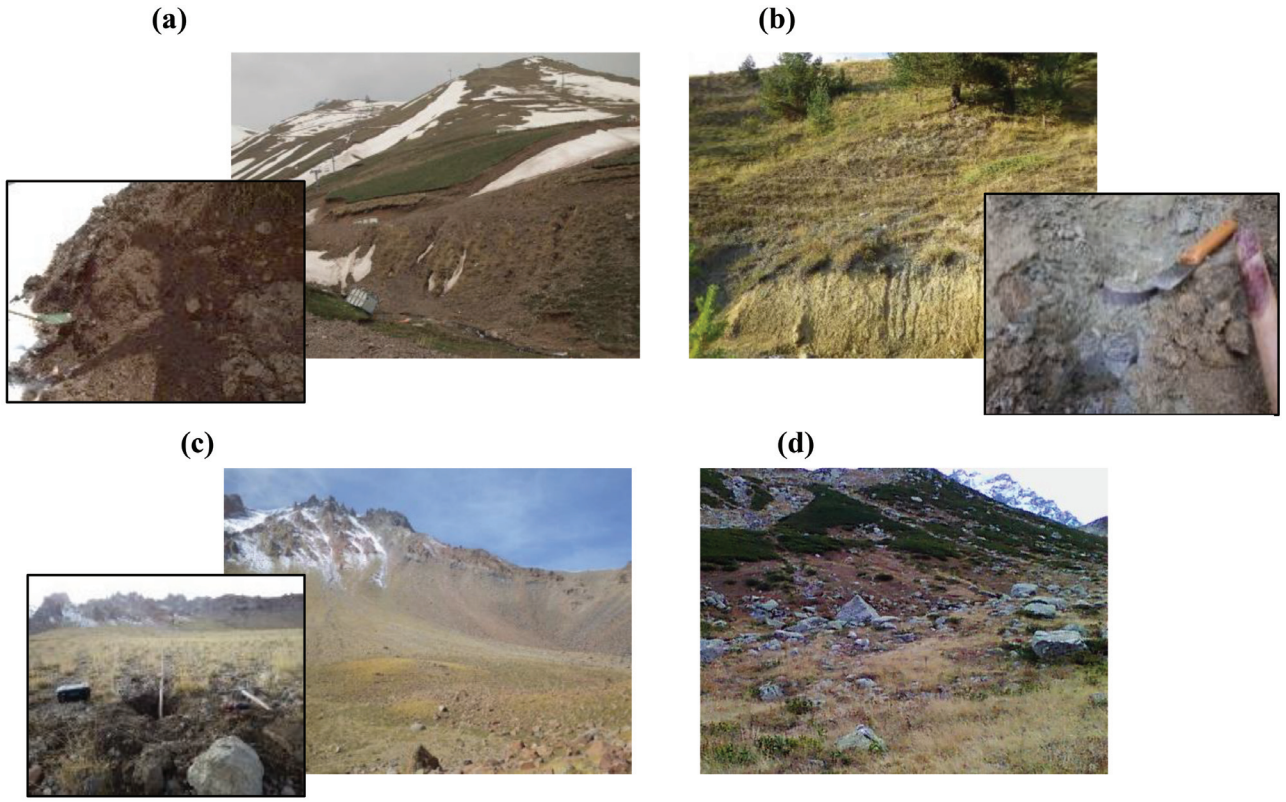


**Fig. 4** Sampling areas: Palandöken Mountain (altitude 3000 m) (a), Ilgaz Mountain (altitude 2000 m) (b), Erciyes Mountain (altitude 3100 m) (c), and Kaçkar Mountain (altitude 2600 m) (d)

pit (Fig. 5c–d). The soil temperature was -2.6°C at a depth of 50 cm (Fig. 5d). Ice needles have also been observed on soil slopes (Fig. 5e–f).

## MATERIALS

At high altitudes, air temperatures are low, the water in the environment is frozen, and physical degradation is more effective than chemical weathering. In mountainous areas, sediment transport typically occurs through glaciers or surface runoff. Thus, angular and coarse-grained soils with little or no clay content were observed in mountainous regions. The grain fractions (Fig. 6, Table 1) and the soil group symbols were determined according to the BS 1377, ASTM D6913, and ASTM D4318-05 standards (Table 2). Grain size and plasticity features were considered when classifying the samples.

The experimental data of the four mountainous areas show that the ratio of coarse grains increases, and the ratio of fine grains decreases with altitude, with an $R^2$ value of 0.53 (Fig. 7).

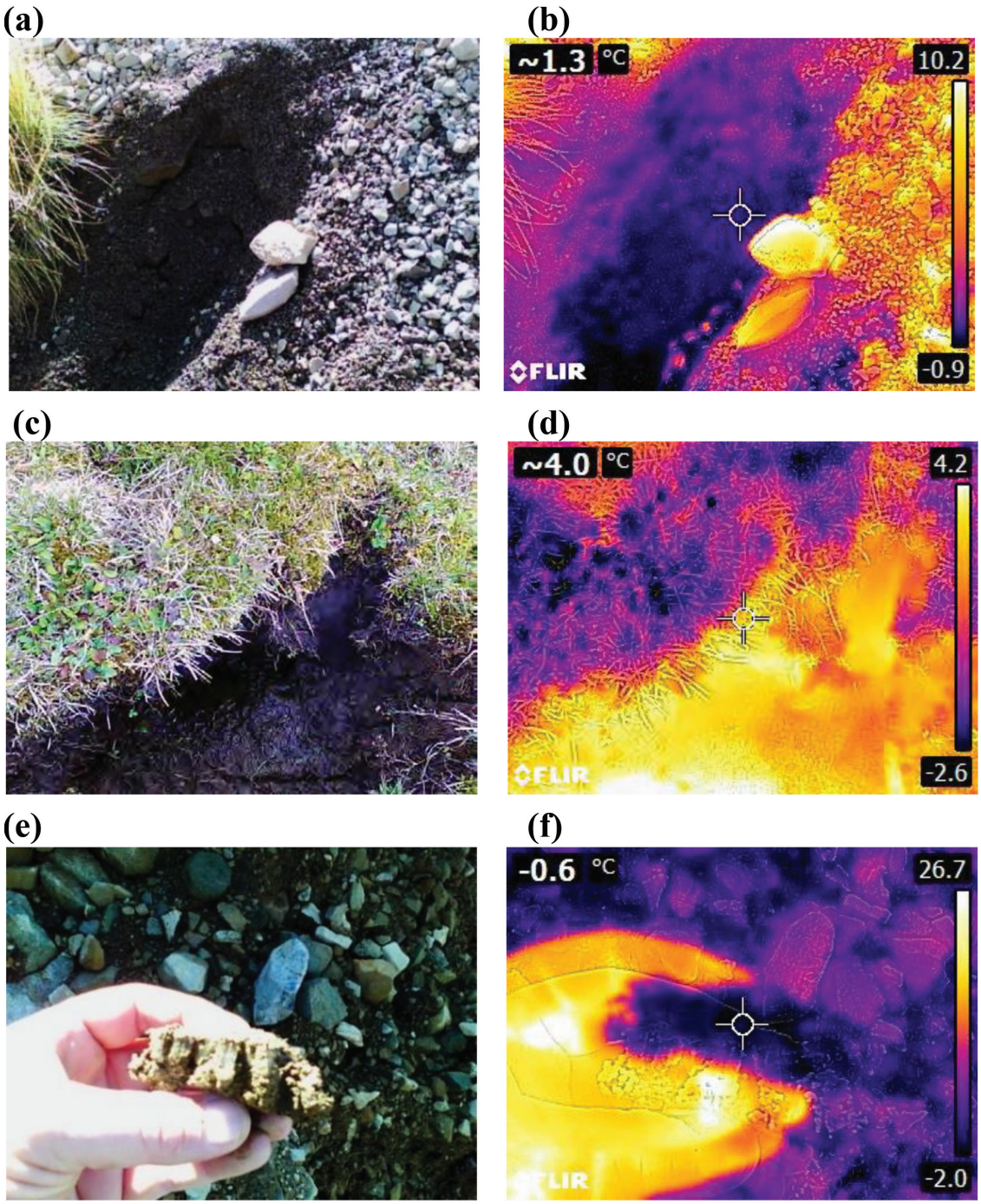


**Fig. 5** Research pit in the Erciyes Mountain (a) and thermal view of the pit (b). Research pit in the Kavron Highlands (Kaçkar Mountain) (c) and its thermal view (d). Ice needles in the soil (Kavron Plateau) (e) and their thermal view (f)

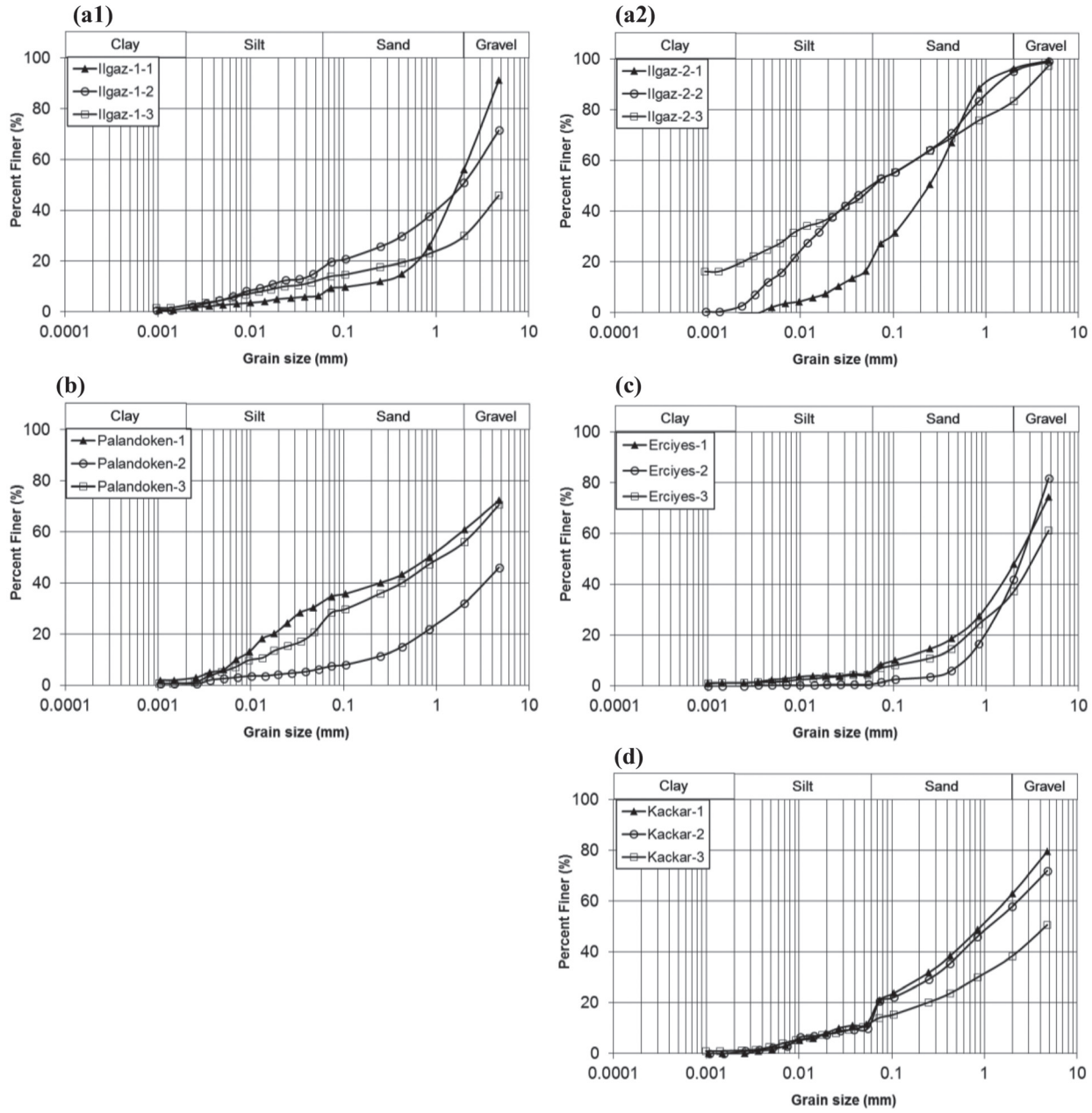


**Fig. 6** Grain size distribution curves of the Ilgaz 1-2 (a1-a2), Palandöken (b), Erciyes (c), and Kaçkar samples (d) (Karamut 2016)

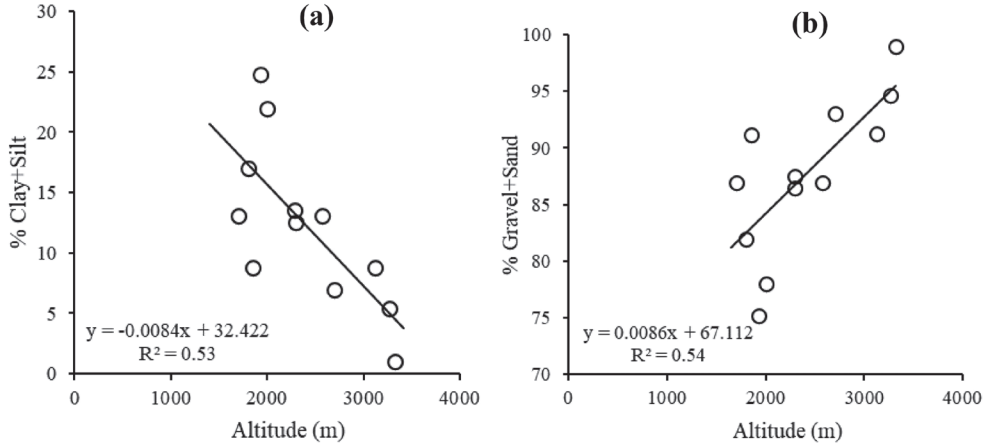


**Fig. 7** The variation in the grain sizes of the soil samples with altitude for clay-silt (a) and sand-gravel (b)

**Table 1** Soil classification according to the BSI standard (Karamut 2016)

| Sample No | Grain (%) | | | |
|---|---|---|---|---|
| | Clay | Silt | Sand | Gravel |
| Palandöken-1 | 2.30 | 29.70 | 28.93 | 39.07 |
| Palandöken-2 | 0.71 | 6.23 | 25.12 | 67.94 |
| Palandöken-3 | 1.03 | 23.81 | 31.13 | 44.03 |
| Ilgaz-1-1 | 1.30 | 7.5 | 56.08 | 35.12 |
| Ilgaz-1-2 | 1.55 | 15.5 | 33.84 | 48.11 |
| Ilgaz-1-3 | 2.2 | 10.9 | 16.77 | 70.13 |
| Ilgaz-2-1 | 0.00 | 22.00 | 74.25 | 3.75 |
| Ilgaz-2-2 | 2.00 | 51.00 | 42.22 | 4.78 |
| Ilgaz-2-3 | 19.00 | 50.00 | 14.46 | 16.54 |
| Erciyes-1 | 1.25 | 7.50 | 39.28 | 51.97 |
| Erciyes-2 | 0.00 | 1.00 | 41.09 | 57.91 |
| Erciyes-3 | 1.10 | 4.26 | 31.86 | 62.78 |
| Kaçkar-1 | 0.00 | 13.50 | 49.53 | 36.97 |
| Kaçkar-2 | 0.93 | 12.17 | 25.29 | 61.61 |
| Kaçkar-3 | 0.50 | 12.00 | 45.41 | 42.09 |

## METHODS

### Laboratory tests

A new device was developed to determine the frost-heaving pressure and the strength of soil samples at low temperatures. The device consisted of two main parts: a cooling unit and a cabinet. The cooling unit had a liquid system, and the specimens were cooled to the desired temperature using a cooling liquid from the antifreeze tank (Fig. 8). The system can provide cooling of up to -20°C.

The cooling cabinet froze the soil sample placed in the cabin through the upper and lower plates. In addition, ambient temperature control can be achieved using a cooling unit inside the cab. A thermal camera was placed on the cover of the cooling cabin (Fig. 9). During the tests, the surface temperatures of the sam-

**Table 2** Physical properties and soil types for the unified soil classification system (USCS)

| Sample/Parameter | w (%) | $G_s$ | LL (%) | PL (%) | PI (%) | <# 200 | Soil type |
|---|---|---|---|---|---|---|---|
| Palandoken-1 | 30.62 | 2.48 | 39.96 | 11.40 | 28.56 | 34.78 | SM |
| Palandoken-2 | 14.95 | 2.47 | 31.59 | 7.75 | 23.84 | 7.55 | GW–GM |
| Palandoken-3 | 18.86 | 2.60 | 36.58 | 11.16 | 25.42 | 28.33 | SM |
| Kackar-1 | 28.06 | 2.48 | 39.96 | 28.57 | 11.39 | 21.03 | SM |
| Kackar-2 | 43.42 | 2.40 | 31.59 | 23.85 | 7.74 | 20.55 | SM |
| Kackar-3 | 16.67 | 2.67 | 36.61 | 25.42 | 11.19 | 14.08 | GM |
| Ilgaz-1-1 | 7.02 | 2.55 | 31.35 | 24.33 | 7.02 | 9.30 | SW–SM |
| Ilgaz-1-2 | 5.45 | 2.79 | 32.42 | 22.29 | 10.13 | 19.77 | SM |
| Ilgaz-1-3 | 3.35 | 2.77 | 31.10 | 24.33 | 6.77 | 14.00 | GM |
| Ilgaz-2-1 | 8.18 | 2.70 | 29.47 | 8.64 | 20.83 | 27.23 | SM |
| Ilgaz-2-2 | 19.17 | 2.87 | 17.77 | 2.00 | 15.77 | 52.94 | ML |
| Ilgaz-2-3 | 7.9 | 2.71 | 33.66 | 22.28 | 11.38 | 52.63 | ML |
| Erciyes-1 | 6.49 | 2.60 | 24.02 | 16.00 | 8.02 | 8.43 | SW–SM |
| Erciyes-2 | 4.34 | 2.62 | – | Non-plastic | – | 1.51 | SW |
| Erciyes-3 | 9.67 | 2.58 | – | Non-plastic | – | 7.00 | SW |

w (%): water content, Gs: specific gravity, LL (%): liquid limit, PL (%) plastic limit, PI (%): plasticity index, <# 200: finer than no. 200%, GW: well graded gravel, GM: silty gravel, SW: well graded sand, SM: silty sand, ML: low plasticity silt.

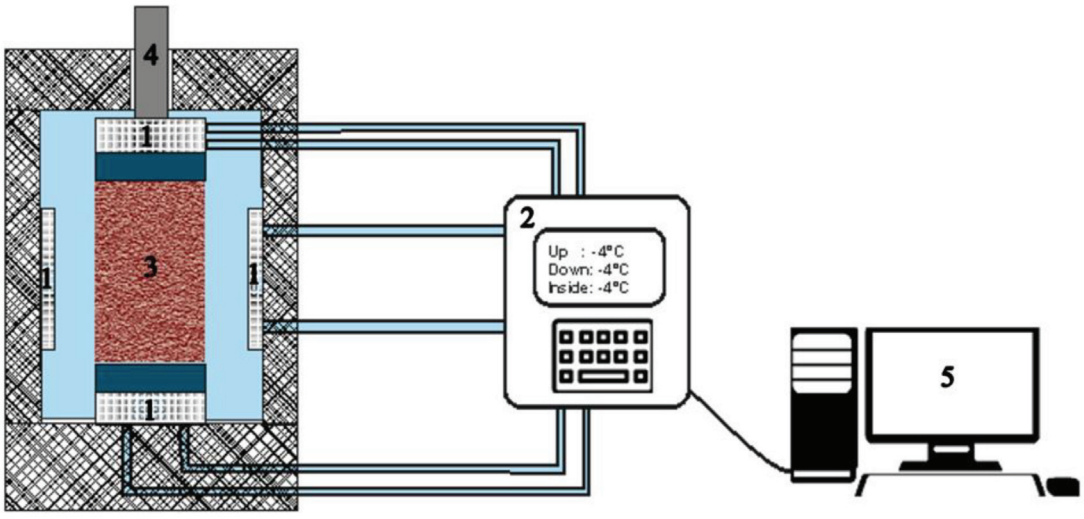


**Fig. 8** Schematic view of the uniaxial frost heaving pressure and strength measurement device: freezing plates (1), liquid cooling system (2), sample (3), piston cylinder (4), controller and PC (5)

ples were measured using a thermal camera focused on the middle of the sample. The uniaxial compressive strength and vertical deformation values of the samples were obtained using a load cell and axial strain transducer at the top of the freezing cabinet (Fig. 9a). The samples were allowed to break for five minutes. The elastic moduli of the samples were calculated from their strength and vertical strain values.

Samples taken from silty soils using sampling tubes (Fig. 4b) were directly used in the experiments. Sandy samples were prepared by compacting them in moulds with a diameter of 5 cm and a height of 10 cm using their natural water content. The specimens were placed in the cooling cabinet of the device in contact with the upper and lower plates. The readings in the pressure display increased over time depending on the volume change. The strength of the frozen samples and vertical deformation were determined to be 0, -4, and -8°C (Fig. 10). Sixty cylindrical samples were tested at each temperature, and 182 samples were examined in total.

**Statistical evaluations**

Multicollinearity analyses were performed to determine the effects of the input variables on the results of the multiple regression analyses (MLR). Multicollinearity is a fundamental concept in MLR, which explains how independent and predictor variables are highly correlated. An 'overlap' or sharing of predictive power may lead to a paradoxical effect, whereby the regression model fits the data well when the independent variables are multicollinear. However, none of the predictor variables significantly affected the prediction of the dependent variables. The dependent variables may not contribute significantly to the model when predictor variables are highly correlated and share information. Multicollinearity was checked using 'tolerance' or the variance inflation factor (VIF). The tolerance value indicates the percentage of variance in the predictor that cannot be accounted for by the other predictors. Values less than 0.10 deserve further investigation (Ho 2006). This value was calculated by subtracting $R^2$ from unity. The VIF measures the extent to which a coefficient's variance (square of the standard error) increases because of collinearity. If it is substantial (i.e., ten or more), collinearity is a severe problem (Ott, Longnecker 2001). Multiple regression analyses were performed using Excel with variables with low VIF values. This study estimated frost resistance and frost heave by using triangle diagrams. Therefore, correlation matrices were created, and the three variables that yielded the highest correlation values with frost resistance and heaving data were determined.

In addition, the standardised coefficients of the variables were calculated to support the results of the correlation matrices. Standardised coefficients allow researchers to compare the relative magnitude of the effects of different explanatory variables in the path model by adjusting the standard deviations such that all the variables, despite other units of measurement, have equal standard deviations. These standardised path coefficients measure the relative strength and sign of the effect of a causal variable on an endogenous or outcome variable in the model. When more than one causal variable is present in the model, the standardised path coefficients represent partial regression coefficients that measure the effect of one variable on another, controlling for prior variables (Llears 2005). XLSTAT software (Addinsoft 2024) was used for the analyses.

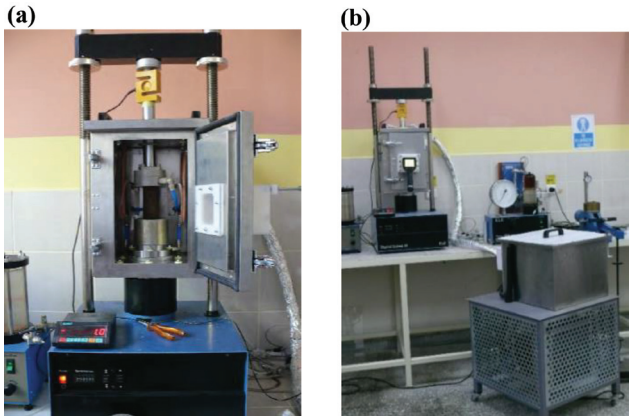


**Fig. 9** Cabinet (a), cooling unit and cabinet (b)

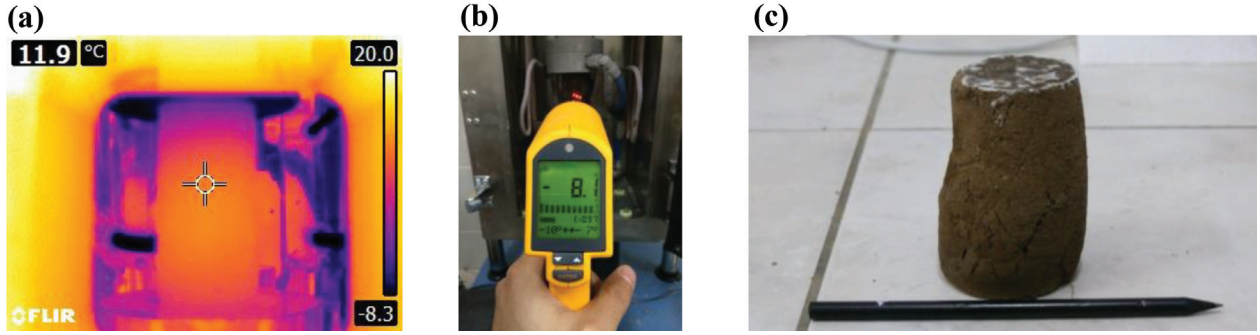


**Fig. 10** Thermal view of the sample during the test (a), IR temperature reading at the end of a uniaxial compressive strength test on frozen soil at a temperature of -8°C (b), and picture of a sample tested (c)

**Artificial Neural Networks**

Artificial neural networks are essentially a type of graph structure with weights. Each node is known to be a neuron. Mathematical operations were performed on the data at each step, considering the weight and bias values in the data transfer among the neurones. Weight and bias values were randomly assigned when an artificial neural network was created, and many epochs were forwarded to determine the optimum weights for solving the problem. Each neuron receives weighted ($W_{ij}$) outputs from the preceding layer in the hidden layer and feeds them over a transfer function to produce neuron input ($N_j$) followed by the targeted output (Eq. 1). This is given by

$$N_J = \sum N_i W_{ij} + \theta_j \quad (1)$$

$N_i$: input data, $\theta_j$: threshold value

The activation function *f (x)* describes the neuron output for the induced local field *x*. In general, linear, hyperbolic tangent, and sigmoid activation functions are used to develop networks for prediction purposes (Haykin 1994). The most used activation function within neurones for complex systems is the logistic sigmoid function, which takes the form (Eq. 2):

$$f(x) = 1 / (1 + e^{-x}) \quad (2)$$

The most popular method for optimising connection weights during network training is the backpropagation neural network (BPNN) developed by Rumelhart *et al.* (1986).This process includes adjusting the weights of the connections in the network to minimise the variation between the output vector predicted ($O_p$) by the trained network and the desired (experimental) output vector ($O_d$). Thus, the global error function (Error) is calculated as

$$\text{Error} = ½ \sum (O_d - O_p)^2 \quad (3)$$

The error in the output layer in the network propagates backwards to the input layer through the hidden layer to obtain the final desired output in the BPNN. The connection weights are adjusted using a form of the generalised delta learning rule to minimise the error function and obtain the desired output from a given set of inputs during the learning process (Rene *et al.* 2009). The data were also normalised and scaled to 0–1 to suit the transfer function in the hidden (sigmoid) and output (linear) layers (Eq. 4) (Binal, Binal 2020).

$$V_n = (V_s - V_{min}) / (V_{max} - V_{min}) \quad (4)$$

$V_n$: normalised value, $V_{min}$: minimum value, $V_{max}$: maximum value, $V_s$: de-normalised value

Linear partitions were observed when triangular diagrams were created using the multiple regression equations. Therefore, it was concluded that graphics in zonation can be obtained through ANN analysis. Before examination, the dataset was divided into two groups: the first set was used as a test set containing 70% of the data, and the second set was used as a validation set of 30%. The percentage of training data should be maintained at a high level to obtain a correct solution. Therefore, the partition ratio for this cluster was defined as 70%. Moreover, the data from all sets were randomly selected from the data list, and Eq. 4 was used to normalise the data. In the neural model, a flexible backpropagation ($R_{prop}$) learning algorithm with five neurons was used in the hidden layer.

**Ternary Charts**

ANN analyses were performed using the three variables determined from the MLP analyses. Ternary diagrams were created based on the ANN analysis results.

A triangle/ternary diagram is a barycentric coordinate of three variables that sum to a constant. It is often used in many fields (physics, metallurgy, petrology, physical chemistry, etc.) to determine system compositions by positioning the ratios of three variables on an equilateral triangular graph. The constant K equals the sum of three variables (a, b, and c) accepted as the input data in the diagram. The sum of these variables was calculated to be 1 or 100. Therefore, the variables whose sum equals the constant "a + b + c = K" cannot be considered independent. Knowing only two variables on a ternary diagram is sufficient to find a point. The most crucial advantage of three-dimensional drawing is that the three variable values can be easily prepared in two dimensions. Thus, triple variables can be used to construct a phase diagram by crossing lines in different directions, where each point represents a different combination of three components. Parallel lines are drawn at regular intervals between the zero edge and vertex, and fine lines can then be removed to estimate the output value quickly. As shown in Fig. 11, the percentage of specific creep decreases linearly with distance from the corner (Binal, Binal 2020; Korkmaz *et al.* 2023).

The values corresponding to 10% of the value of each variable in the ternary diagram were estimated using ANN analysis. These data were subsequently contoured using the MATLAB 2020 software. A ternary diagram was created using the estimated equality obtained from the multiple regression analyses of the T°C, < 200%, and w% variables. However, no zoning occurred in the diagram because the multiple regressions showed a linear relationship. Therefore, ternary diagrams were created based on the results of the ANN analysis (Binal, Binal 2020). The use of the chart is explained item by item as follows:

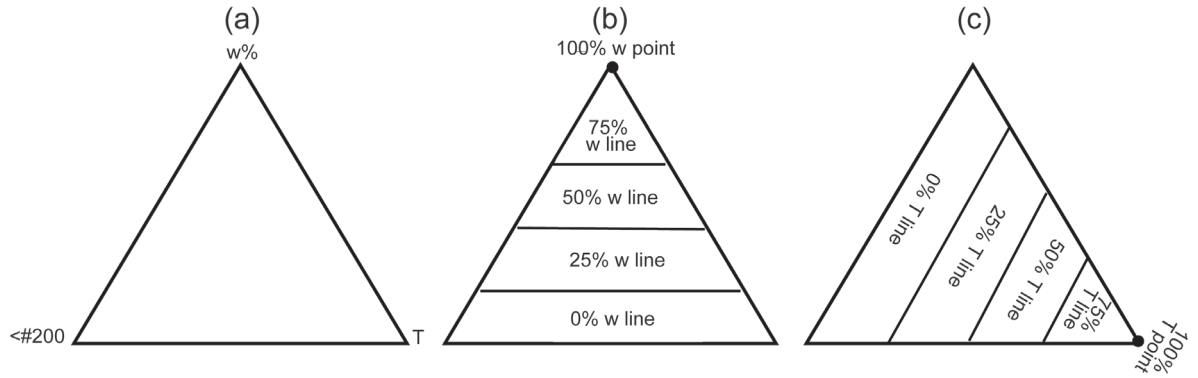


**Fig. 11** Example ternary diagram without any points plotted (a), ternary diagram showing increases along the first axis (b), ternary diagram showing increases along the third axis (c)

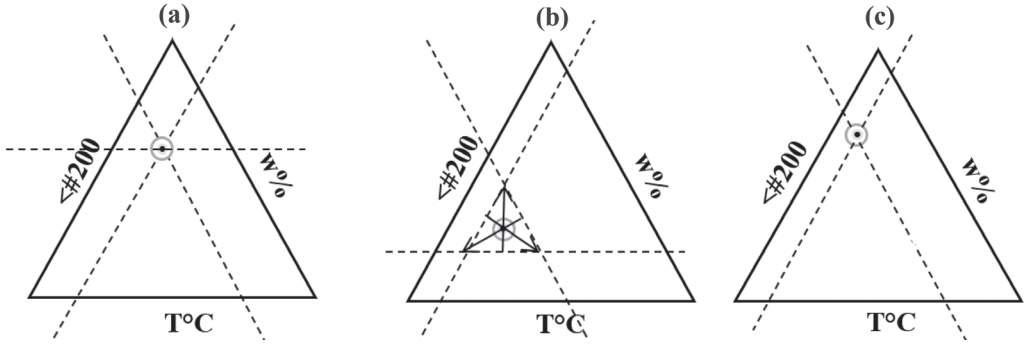


**Fig. 12** Use of ternary diagram: point of concurrency (a), centroid of triangle of non-concurrent lines that do not intersect at a single point (b), and two-line intersection (c)

(1) The horizontal line contains the same parameters between the edges;

(2) The same operations were applied to the edges containing other parameters;

(3) If the intersection of the lines in the ternary diagram coincides with a point, this point provides the estimated value (Fig. 12a);

(4) When the intersection of the lines in the ternary diagram forms a triangle, the centre point of the resulting triangle provides an estimated value (Fig. 12b);

(5) The intersection in the ternary diagram (Fig. 12c) indicates the estimated values.

## RESULTS

Experiments have shown that soil samples exhibit different behaviours at low temperatures depending on the grain size distribution and water content. As the amount of fine-grained material in the soil sample increased, the frost-heaving pressure also increased (Table 3, Fig. 13a). This determination is explained by the fact that the fine material holds water and causes more frost-swelling pressure because of freezing. Water in the soil pores can drain quickly in coarse-grained soils. In addition, ice that expands because of freezing in large gaps between coarse grains does not create a significant internal pressure, even if its volume increases. The frost-heaving pressure rises as the temperature drops, reaching 31.48 kPa in samples with excess clay content. Furthermore, the frost-heaving pressure increased with the water content (Fig. 13b). At temperatures below zero, the water movement in the pores decreased, and the frost-heaving pressure increased with the volume of ice formed in the pores. The strength of the soil samples increased depending on the fine-particle content (Fig.14a, Tables 4–5). The same behaviour was observed for the water content (Fig. 14b). Freeze-thaw cycles transform the fine and medium pores of coarse-grained soil into large pores, and the ratio of the pore volume of large pores gradually increases, which destroys the cementation ability between the soil particles in coarse-grained soil and reduces its strength (Liu *et al.* 2022). The same behaviour was observed in this study; however, the strength of the soil samples decreased with increasing test temperature (Fig. 15).

As the soil water content increased, the ice resistance in the pores and modulus of elasticity increased at low temperatures. Ice behaviour becomes significant at low temperatures and high water contents, whereas soil strength is important at low temperatures. Therefore, no meaningful relationships were found among the modulus of elasticity, water content, or fine-grain ratio (Fig. 16a–b)

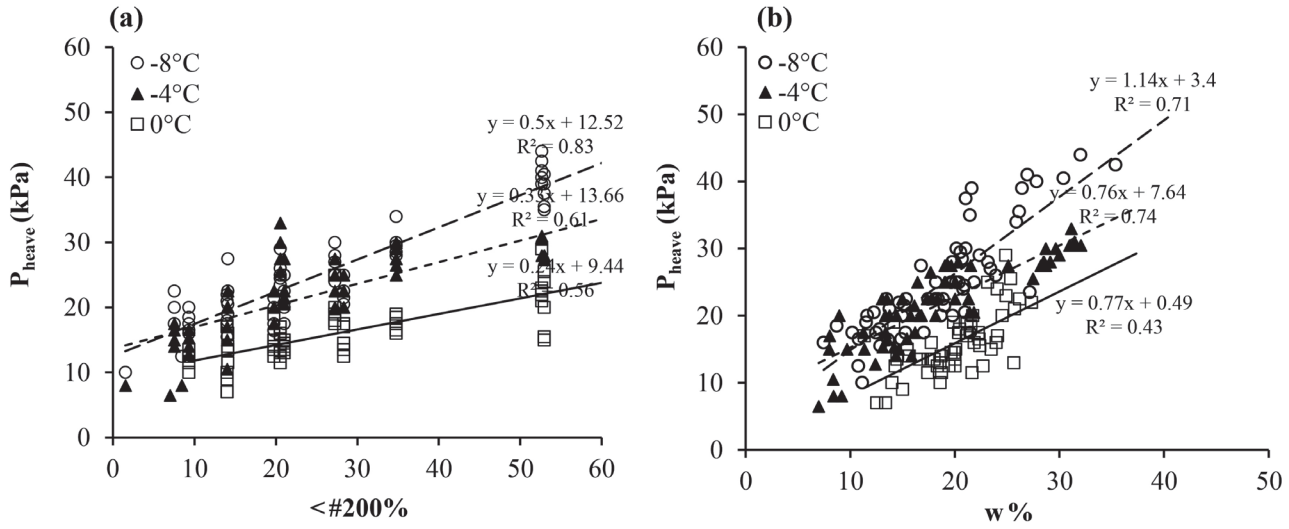


**Fig. 13** Frost heaving pressure ($P_{heave}$) *vs*. fine grain content (< #200) (a) and frost heaving ($P_{heave}$) *vs*. water content (w%) (b)

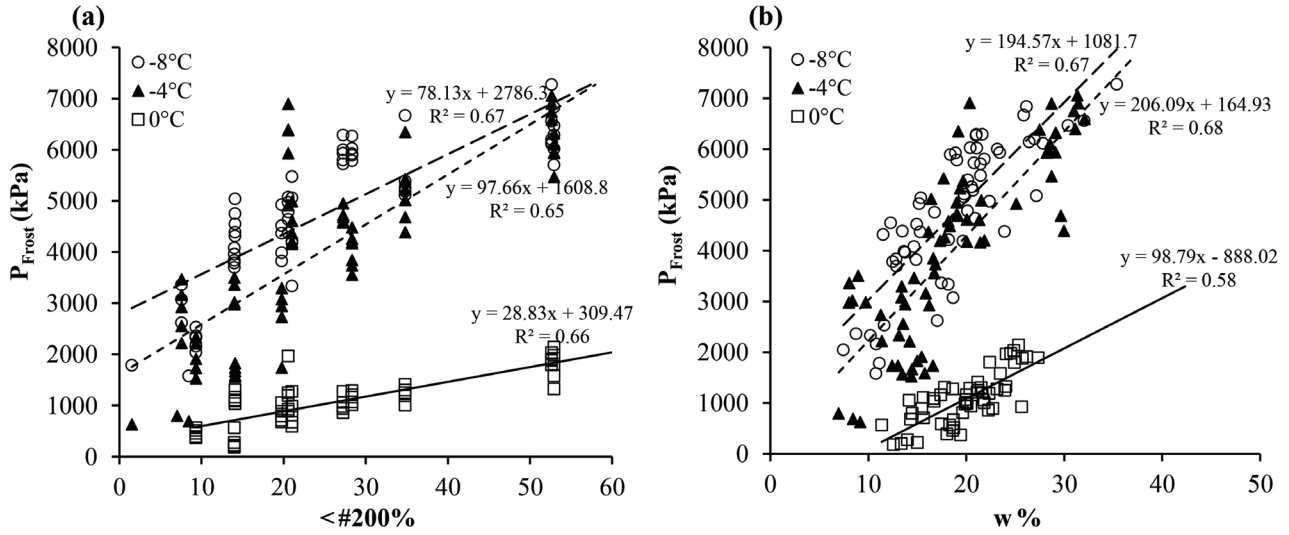


**Fig. 14** Frost strength ($P_{frost}$) *vs*. fine grain content (a), frost strength ($P_{frost}$) *vs*. water content (b)

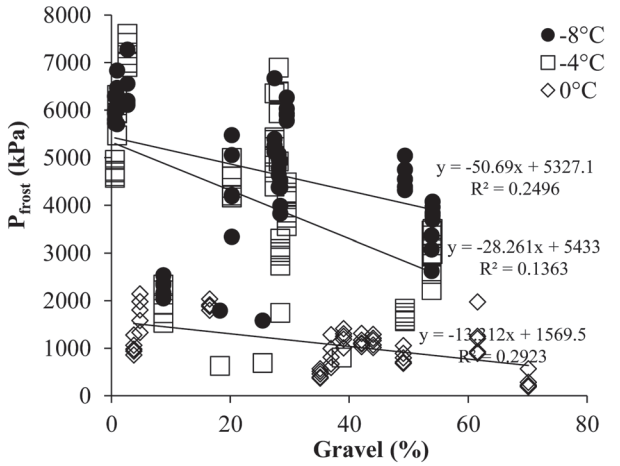


**Fig. 15** Uniaxial compressive strength ($P_{frost}$) dependence on temperature and gravel content

## Analyses

The frost-heaving pressure ($P_{heave}$), compressive strength ($P_{frost}$), and elasticity modulus (E) estimation equations were developed using multiple regression analyses based on the physical properties of the soil samples (Eqs 1–3). A total of 182 data points were used for each variable. The PL and LL values could not be determined for Erciyes 2–3 because the clay content of the Erciyes soil samples was too low. Therefore, the minimum values for Erciyes soil samples were set to zero (Table 6). The VIF is the inverse of tolerance (i.e. 1/tolerance). The multicollinearity effect was determined for LL (Table 7). This variable should not be combined with other Atterberg limit variables in the MLR analysis. The root mean square deviation (RMSE) measures the standard deviation of the MLR model error, and Akaike information criterion (AIC)

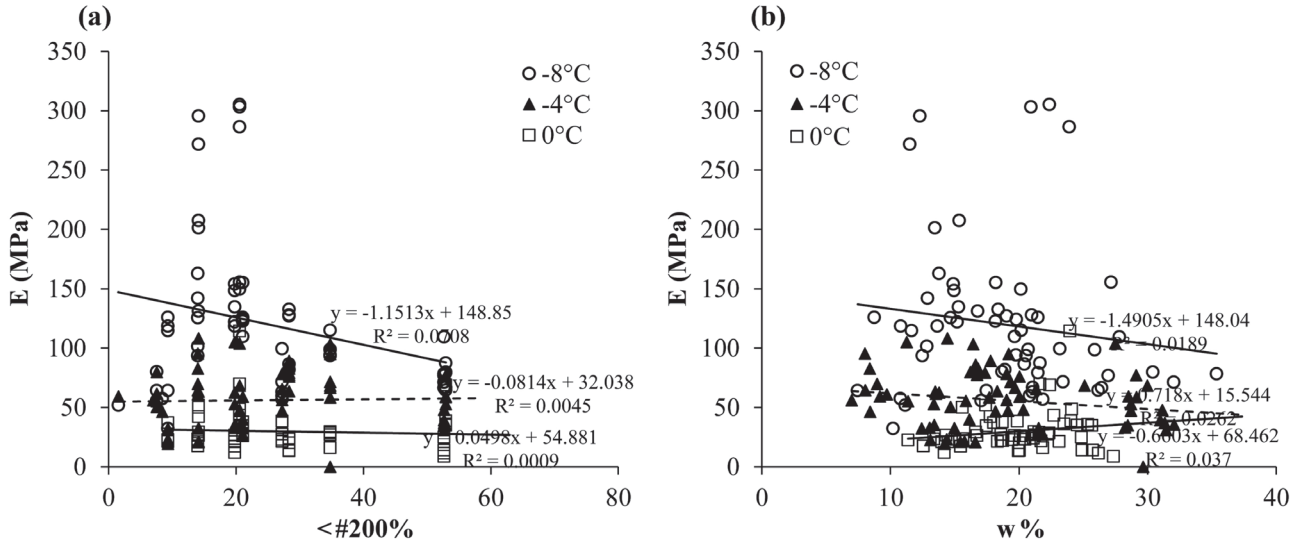


**Fig. 16** Elasticity modulus *vs*. fine grain content (a) and elasticity modulus *vs.* water content (b)

**Table 3** Frost heaving pressures ($P_{heave}$)

| T ($^0$C) | Location | Max (kPa) | Min (kPa) | $\bar{x}$ (kPa) | σ (kPa) | N |
|---|---|---|---|---|---|---|
| 0 | Palandoken | 19.0 | 12.5 | 16.3 | 1.8 | 10 |
| 0 | Kackar | 17.0 | 11.5 | 14.0 | 1.6 | 15 |
| 0 | Ilgaz-1 | 19.0 | 10.0 | 13.4 | 1.9 | 15 |
| 0 | Ilgaz-2 | 25.5 | 15.0 | 20.0 | 3.9 | 15 |
| -4 | Palandoken | 30.0 | 14.0 | 21.6 | 1.5 | 19 |
| -4 | Kackar | 33.0 | 20.5 | 25.6 | 2.9 | 15 |
| -4 | Ilgaz-1 | 22.5 | 12.7 | 17.2 | 1.8 | 15 |
| -4 | Ilgaz-2 | 28.0 | 20.0 | 26.0 | 1.5 | 15 |
| -4 | Erciyes1 | 8.0 | 6.5 | 7.5 | 0.9 | 2 |
| -8 | Palandoken | 34.0 | 17.5 | 25.0 | 2.5 | 13 |
| -8 | Kackar | 29.0 | 17.5 | 23.8 | 2.7 | 15 |
| -8 | Ilgaz-1 | 21.5 | 16.0 | 18.1 | 2.0 | 15 |
| -8 | Ilgaz-2 | 40.5 | 24.0 | 32.2 | 2.4 | 15 |
| -8 | Erciyes1 | 12.5 | 10.0 | 11.2 | 1.8 | 2 |

Max: maximum, Min: minimum, $\bar{x}$: average, σ: standard deviation, N: sample number.

**Table 4** Uniaxial compressive strength ($P_{frost}$) under low-temperature conditions

| T ($^0$C) | Location | Max (kPa) | Min (kPa) | $\bar{x}$ (kPa) | σ (kPa) | N |
|---|---|---|---|---|---|---|
| 0 | Palandoken | 1408.9 | 1006.7 | 1189.6 | 129.8 | 10 |
| 0 | Kackar | 1968.5 | 589.6 | 1056.7 | 355.1 | 15 |
| 0 | Ilgaz-1 | 1054.2 | 369.7 | 642.5 | 117.0 | 15 |
| 0 | Ilgaz-2 | 2138.4 | 859.3 | 1393.7 | 239.8 | 15 |
| -4 | Palandoken | 6350.2 | 2223.3 | 4039.4 | 558.3 | 19 |
| -4 | Kackar | 6894.7 | 4161.8 | 5285.5 | 543.4 | 15 |
| -4 | Ilgaz-1 | 3297.5 | 1529.4 | 2353.0 | 470.5 | 15 |
| -4 | Ilgaz-2 | 6320.2 | 4576.5 | 5332.5 | 231.2 | 15 |
| -4 | Erciyes 1 | 799.4 | 629.5 | 706.1 | 86.2 | 2 |
| -8 | Palandoken | 6669.9 | 2618.0 | 4270.8 | 512.0 | 13 |
| -8 | Kackar | 5475.8 | 3337.5 | 4611.8 | 555.6 | 15 |
| -8 | Ilgaz-1 | 4926.2 | 2043.4 | 3305.3 | 313.7 | 15 |
| -8 | Ilgaz-2 | 6832.3 | 5705.7 | 6105.1 | 323.9 | 15 |
| -8 | Erciyes 2 | 1786.1 | 1578.8 | 1682.5 | 146.6 | 2 |

**Table 5** Elasticity moduli (E)

| T ($^0$C) | Location | Max (kPa) | Min (kPa) | $\bar{x}$ (kPa) | σ (kPa) | N |
|---|---|---|---|---|---|---|
| 0 | Palandoken | 29.7 | 13.6 | 22.6 | 5.4 | 10 |
| 0 | Kackar | 114.3 | 26.1 | 46.3 | 18.7 | 15 |
| 0 | Ilgaz-1 | 37.3 | 12.0 | 22.7 | 6.2 | 15 |
| 0 | Ilgaz-2 | 68.8 | 21.4 | 34.7 | 10.9 | 15 |
| -4 | Palandoken | 103.3 | 50.5 | 69.3 | 15.6 | 19 |
| -4 | Kackar | 108.3 | 27.2 | 53.5 | 17.4 | 15 |
| -4 | Ilgaz-1 | 105.0 | 19.4 | 46.6 | 16.7 | 15 |
| -4 | Ilgaz-2 | 77.3 | 34.9 | 54.6 | 11.3 | 15 |
| -4 | Erciyes 1 | 59.2 | 42.9 | 52.7 | 8.6 | 2 |
| -8 | Palandoken | 114.9 | 55.6 | 83.4 | 10.6 | 13 |
| -8 | Kackar | 305.0 | 109.8 | 183.7 | 48.5 | 15 |
| -8 | Ilgaz-1 | 154.0 | 32.1 | 113.4 | 28.3 | 15 |
| -8 | Ilgaz-2 | 99.4 | 56.8 | 72.8 | 13.5 | 15 |
| -8 | Erciyes 2 | 57.4 | 51.8 | 54.6 | 3.9 | 2 |

is the variance in the MLR model adjusted for the sample size and number of parameters. Furthermore, RMSE, AIC, and $R^2$ measure the goodness-of-fit and aid in selecting a well-fitted model (Table 8).

The MLR equation for the swell pressure was estimated using a high correlation coefficient ($R^2 = 0.801$). At -4°C, frozen water was more effective than soil particles. Therefore, the lowest $R^2$ values were determined for elasticity modulus estimation. The estimation equations for $P_{heave}$, $P_{frost}$, and E are given in Eqs 5–7. (T: temperature, w: natural water content, <# 200: percentage passing through No. 200, LL: liquid limit):

$$P_{heave} = 1.82–1.25*T + 0.47*w + 0.19* <\#\ 200–0.02E^{-02} *Sand–0.038E^{-02} *Gravel + 0.072* LL \quad (5)$$

$$P_{frost} = -1711.3–482.3* T + 113.7* w + 27.64* <\#\ 200–3.09* Sand–14.89* Gravel + 28.55* LL \quad (6)$$

**Table 6** Statistical evaluation of the variables

| Location | Parameter | Max (%) | Min (%) | Average | σ | N |
|---|---|---|---|---|---|---|
| Palandoken | w (%) | 29.98 | 11.37 | 19.41 | 3.47 | 42 |
| | <# 200 (%) | 34.78 | 7.55 | 26.98 | 9.98 | 42 |
| | Sand (%) | 31.13 | 25.12 | 29.09 | 2.19 | 42 |
| | Gravel (%) | 67.94 | 39.07 | 37.00 | 10.73 | 42 |
| | LL (%) | 39.96 | 31.59 | 37.00 | 3.07 | 42 |
| | PL (%) | 11.40 | 7.75 | 10.61 | 1.41 | 42 |
| | PI (%) | 28.56 | 23.84 | 26.39 | 1.90 | 42 |
| | Ac | 3.16 | 0.82 | 1.30 | 0.91 | 42 |
| Kackar | w (%) | 31.14 | 11.52 | 19.89 | 4.59 | 45 |
| | <# 200 (%) | 21.03 | 14.08 | 18.55 | 3.21 | 45 |
| | Sand (%) | 56.08 | 16.77 | 38.57 | 13.02 | 45 |
| | Gravel (%) | 70.13 | 35.12 | 34.58 | 12.34 | 45 |
| | LL (%) | 39.96 | 31.10 | 34.58 | 3.56 | 45 |
| | PL (%) | 28.57 | 22.29 | 25.18 | 2.03 | 45 |
| | PI (%) | 11.39 | 6.77 | 9.40 | 1.94 | 45 |
| | Ac | 0.79 | 0.33 | 0.53 | 0.16 | 45 |
| Ilgaz | w (%) | 35.37 | 7.46 | 19.15 | 6.88 | 90 |
| | <# 200 (%) | 52.94 | 9.30 | 29.31 | 17.57 | 90 |
| | Sand (%) | 74.25 | 14.46 | 40.36 | 17.29 | 90 |
| | Gravel (%) | 70.13 | 3.75 | 30.03 | 23.35 | 90 |
| | LL (%) | 39.96 | 17.77 | 30.03 | 6.06 | 90 |
| | PL (%) | 28.57 | 0.00 | 17.36 | 9.72 | 90 |
| | PI (%) | 20.83 | 0.00 | 9.71 | 6.29 | 90 |
| | Ac | 2.24 | 0.00 | 0.54 | 0.54 | 90 |
| Erciyes | w (%) | 11.15 | 10.79 | 10.97 | 0.25 | 5 |
| | <# 200 (%) | 8.43 | 1.51 | 5.65 | 4.89 | 5 |
| | Sand (%) | 80.26 | 54.26 | 66.88 | 13.01 | 5 |
| | Gravel (%) | 38.75 | 18.23 | 27.47 | 10.41 | 5 |
| | LL (%) | 24.02 | 0.00 | 0.00 | 0.00 | 5 |
| | PL (%) | 16.00 | 0.00 | 0.00 | 0.00 | 5 |
| | PI (%) | 8.02 | 0.00 | 0.00 | 0.00 | 5 |
| | Ac | 0.95 | 0.00 | 0.00 | 0.00 | 5 |

$$E = -27.30–11.36^{*} T + 0.69^{*} w – 0.33^{*} <\#\ 200 + 0.08^{*} Sand + 0.46^{*} Gravel + 0.77^{*} LL \quad (7)$$

Furthermore, correlation matrices showing the relationship between the variables and the target value were created, and the best correlation values among the variables were found between temperature (T), soil water content (w%), and fine grain ratio (<# 200) (Table 9a–c).

The ternary diagrams included three variables. Therefore, more effective variables for the estimation outputs were determined via the MLR analysis. Temperature (T), soil moisture content (w%), and fine grain ratio (<# 200) were defined as the most influential variables for correlation matrices and standardised coefficient examinations (Fig. 17). Therefore, these parameters were selected for the Pheave and Pfrost ternary diagrams. Although all the variables were used in the MLR analysis, the elasticity modulus prediction equation performed poorly. The three-variable MLR analysis was insufficient for estimating the elasticity modulus. Therefore, a ternary diagram was not developed for elasticity modulus prediction.

Three parameters were selected for the input layer: T, w, and <# 200 (Fig. 18a). Pheave and Pfrost were chosen as the output layers. The RMSE of the test procedure is 2.92.

The correlation coefficient ($R^2 = 0.842$) indicated

**Table 7** Multicollinearity statistics

| | T | w% | <# 200 | Sand | Gravel | LL | PL | PI | Ac |
|---|---|---|---|---|---|---|---|---|---|
| Tolerance | 0.987 | 0.411 | 0.249 | 0.507 | 0.390 | 0.097 | 0.121 | 0.139 | 0.393 |
| VIF | 1.013 | 2.433 | 4.012 | 1.973 | 2.564 | 10.299 | 8.233 | 7.190 | 2.542 |

T: test temperature, w (%): water content, Ac: clay activity.

**Table 8** Goodness-of-fit statistics for the equation

| | Data number for each variable | DF | $R^2$ | Adjusted $R^2$ | RMSE | AIC |
|---|---|---|---|---|---|---|
| $P_{heave}$ | 182 | 6 | 0.801 | 0.794 | 3.35 | 446.63 |
| $P_{frost}$ | 182 | 6 | 0.807 | 0.801 | 916.41 | 2489.51 |
| E | 182 | 6 | 0.491 | 0.473 | 39.65 | 1346.44 |

DF: degrees of freedom.

**Table 9a** Correlation matrix for $P_{heave}$

| | T | w | <# 200 | Sand | Gravel | LL | PL | PI | $A_c$ | $P_{heave}$ |
|---|---|---|---|---|---|---|---|---|---|---|
| T | **1** | 0.073 | 0.046 | 0.014 | –0.039 | 0.058 | 0.048 | –0.004 | –0.015 | –0.488 |
| w | 0.073 | **1** | 0.751 | –0.150 | –0.243 | 0.084 | -0.083 | 0.061 | –0.260 | 0.655 |
| <# 200 | 0.046 | 0.751 | **1** | –0.247 | –0.306 | 0.004 | –0.176 | -0.005 | –0.470 | 0.676 |
| Sand | 0.014 | –0.150 | –0.247 | **1** | –0.540 | –0.118 | –0.153 | 0.002 | 0.100 | –0.151 |
| Gravel | –0.039 | –0.243 | –0.306 | –0.540 | **1** | 0.201 | 0.411 | 0.032 | 0.164 | –0.252 |
| LL | 0.058 | 0.084 | 0.004 | –0.118 | 0.201 | **1** | 0.579 | 0.601 | 0.293 | 0.062 |
| PL | 0.048 | –0.083 | –0.176 | –0.153 | 0.411 | 0.579 | **1** | –0.198 | –0.149 | –0.107 |
| PI | –0.004 | 0.061 | –0.005 | 0.002 | 0.032 | 0.601 | –0.198 | **1** | 0.592 | 0.037 |
| Ac | –0.015 | –0.260 | –0.470 | 0.100 | 0.164 | 0.293 | –0.149 | 0.592 | **1** | –0.278 |
| $P_{heave}$ | –0.488 | 0.655 | 0.676 | –0.151 | –0.252 | 0.062 | –0.107 | 0.037 | –0.278 | **1** |

**Table 9b** Correlation matrix for $P_{frost}$

| | T | w | <# 200 | Sand | Gravel | LL | PL | PI | Ac | $P_{frost}$ |
|---|---|---|---|---|---|---|---|---|---|---|
| T | **1** | 0.073 | 0.046 | 0.014 | –0.039 | 0.058 | 0.048 | –0.004 | –0.015 | –0.704 |
| w | 0.073 | **1** | 0.751 | –0.150 | –0.243 | 0.084 | –0.083 | 0.061 | –0.260 | 0.463 |
| <# 200 | 0.046 | 0.751 | **1** | –0.247 | –0.306 | 0.004 | –0.176 | –0.005 | –0.470 | 0.455 |
| Sand | 0.014 | –0.150 | –0.247 | **1** | –0.540 | –0.118 | –0.153 | 0.002 | 0.100 | –0.064 |
| Gravel | –0.039 | –0.243 | –0.306 | –0.540 | **1** | 0.201 | 0.411 | 0.032 | 0.164 | –0.222 |
| LL | 0.058 | 0.084 | 0.004 | –0.118 | 0.201 | **1** | 0.579 | 0.601 | 0.293 | 0.066 |
| PL | 0.048 | –0.083 | –0.176 | –0.153 | 0.411 | 0.579 | **1** | –0.198 | –0.149 | –0.141 |
| PI | –0.004 | 0.061 | –0.005 | 0.002 | 0.032 | 0.601 | –0.198 | **1** | 0.592 | 0.125 |
| Ac | –0.015 | –0.260 | –0.470 | 0.100 | 0.164 | 0.293 | –0.149 | 0.592 | **1** | –0.157 |
| $P_{frost}$ | –0.704 | 0.463 | 0.455 | –0.064 | –0.222 | 0.066 | –0.141 | 0.125 | –0.157 | **1** |

**Table 9c** Correlation matrix for the elastic modulus (E)

| | T | w | <# 200 | Sand | Gravel | LL | PL | PI | Ac | E |
|---|---|---|---|---|---|---|---|---|---|---|
| T | **1** | 0.073 | 0.046 | 0.014 | –0.039 | 0.058 | 0.048 | –0.004 | –0.015 | –0.661 |
| w | 0.073 | **1** | 0.751 | –0.150 | –0.243 | 0.084 | –0.083 | 0.061 | –0.260 | –0.078 |
| <# 200 | 0.046 | 0.751 | **1** | –0.247 | –0.306 | 0.004 | –0.176 | –0.005 | –0.470 | –0.121 |
| Sand | 0.014 | –0.150 | –0.247 | **1** | –0.540 | –0.118 | –0.153 | 0.002 | 0.100 | –0.082 |
| Gravel | –0.039 | –0.243 | –0.306 | –0.540 | **1** | 0.201 | 0.411 | 0.032 | 0.164 | 0.218 |
| LL | 0.058 | 0.084 | 0.004 | –0.118 | 0.201 | **1** | 0.579 | 0.601 | 0.293 | 0.110 |
| PL | 0.048 | –0.083 | –0.176 | –0.153 | 0.411 | 0.579 | **1** | –0.198 | –0.149 | 0.160 |
| PI | –0.004 | 0.061 | –0.005 | 0.002 | 0.032 | 0.601 | –0.198 | **1** | 0.592 | –0.012 |
| Ac | –0.015 | –0.260 | –0.470 | 0.100 | 0.164 | 0.293 | –0.149 | 0.592 | **1** | –0.030 |
| E | –0.661 | –0.078 | –0.121 | –0.082 | 0.218 | 0.110 | 0.160 | –0.012 | –0.030 | **1** |

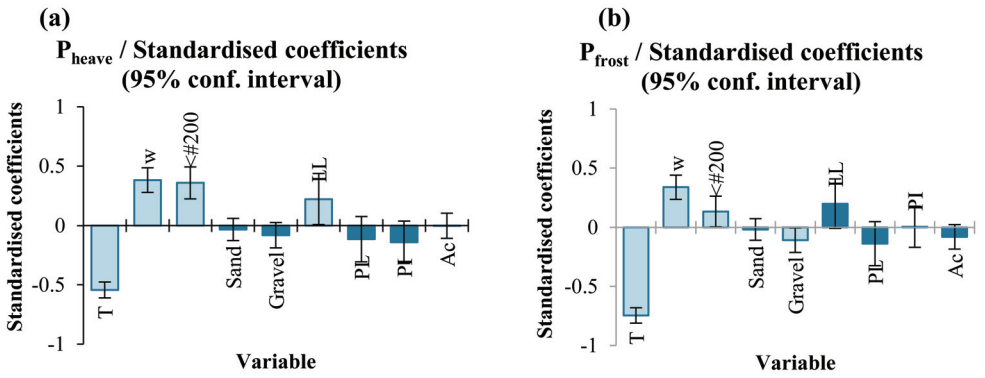


**Fig. 17** Standardised coefficients of variables for $P_{heave}$ (a) and $P_{frost}$ (b)

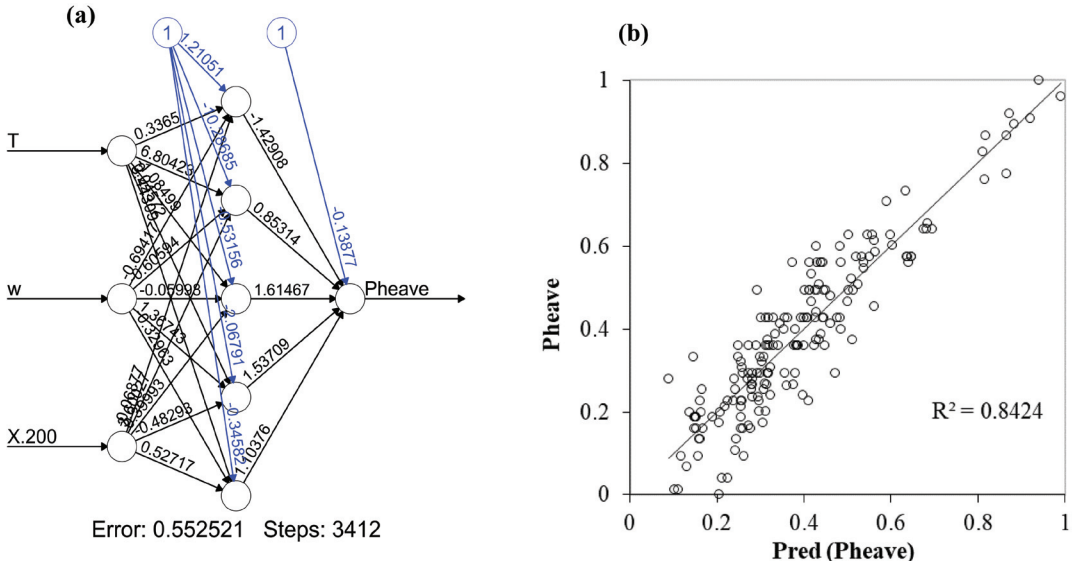


**Fig. 18** Neural network model for $P_{heave}$ estimation (a), relationships between the predicted $P_{heave}$ data and test data (b)

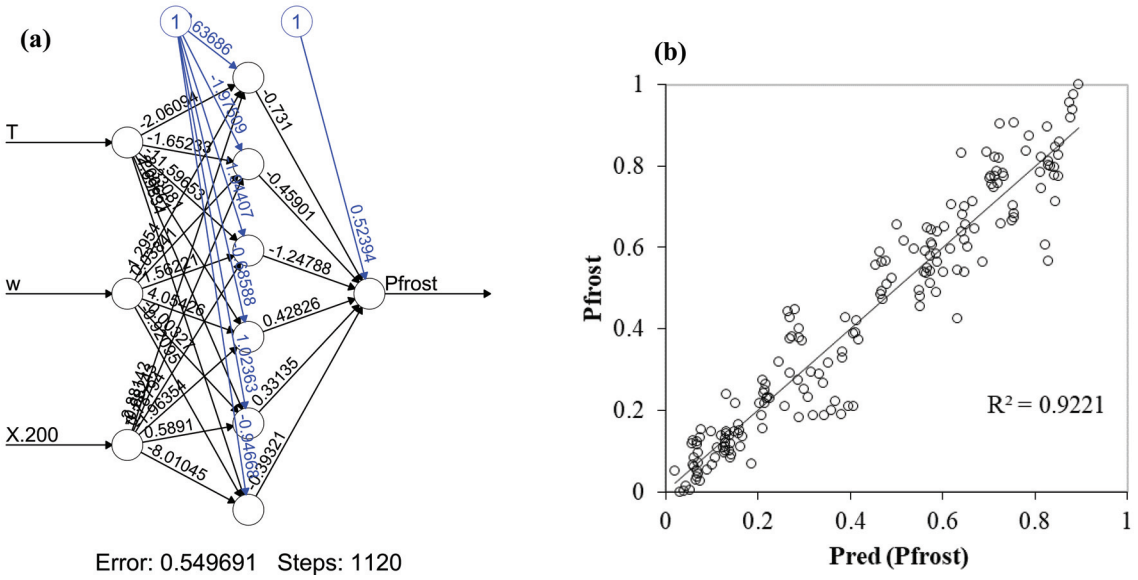


**Fig. 19** Neural network model for estimating $P_{frost}$ (a), relationship between the predicted $P_{frost}$ data and test data (b)

**Table 10** Weights of the artificial network for $P_{heave}$

| Neuron no/ Weights of | 1 | 2 | 3 | 4 | 5 | |
|---|---|---|---|---|---|---|
| Intercept | 1.211 | –10.287 | –0.532 | –2.068 | –0.346 | |
| T | 0.337 | 6.804 | –1.085 | 0.046 | 3.443 | |
| w | –0.694 | –0.606 | –0.060 | 1.367 | –0.330 | |
| <# 200 | –0.069 | 3.600 | 0.400 | –0.483 | 0.527 | Intercept |
| To $P_{heave}$ | –1.429 | 0.853 | 1.615 | 1.537 | 1.104 | –0.139 |

**Table 11** Weights of the artificial network for $P_{frost}$

| Neuron no/ Weights of | 1 | 2 | 3 | 4 | 5 | 6 | |
|---|---|---|---|---|---|---|---|
| Intercept | 2.637 | –1.975 | –1.944 | –0.686 | 1.024 | –0.947 | |
| T | –2.061 | –1.652 | –11.597 | –3.331 | 2.067 | 1.698 | |
| w | –1.295 | 0.038 | 1.562 | 4.054 | –0.003 | –0.921 | |
| <# 200 | –2.881 | –0.682 | 0.788 | –1.964 | 0.589 | –8.010 | Intercept |
| To $P_{frost}$ | –0.731 | –0.459 | –1.248 | 0.428 | 0.331 | –0.393 | 0.524 |

the accuracy of the predicted model (Fig. 18b). Furthermore, the same ANN method and six neurones were used to estimate the strength of frozen samples (Fig. 19a). For the test data, the RMSE was calculated as 576. The $R^2$ value between the actual and predicted data is 0.922 (Fig. 19b). At the end of the iterations, the network weights, which included five neurones, were determined to estimate the Pheave (Table 10). The weights and intercepts of the network for estimating Pfrost were calculated and presented in Table 11.

## Ternary diagrams

The links between the results were investigated using the artificial neural network method, and triangle diagrams based on frost strength and frost heaving were created. Values with the highest correlation obtained using the flexible calculation method were chosen at the edges of the ternary diagrams. The frost pressure-centred triangles formed according to the temperature, fine particle ratio, and water content parameters at 0°C, -4°C and -8°C temperature values are given below (Fig. 20). The Pfrost graph shows that as the soil water content increases and the temperature decreases, the resistance of the soil material increases owing to freezing. The $P_{heave}$ graph showed that water content was the most critical factor influencing soil heaving pressure. Beyond the water content, the fine-grained ratio also influences the swelling pressure (Fig. 21).

## Performance of the diagrams

The water content and fine particle percentage in the ternary diagram controlling the estimation performance of the Pfrost and Pheave values are shown in Fig. 22a–b. The goodness-of-fit of the ternary diagrams is shown in Table 12. These charts present highly reasonable results (for Pfrost, $R^2 = 0.81$; for Pheave, $R^2 = 0.90$). Additionally, the experimental and predictive datasets for the ternary diagrams were similar.

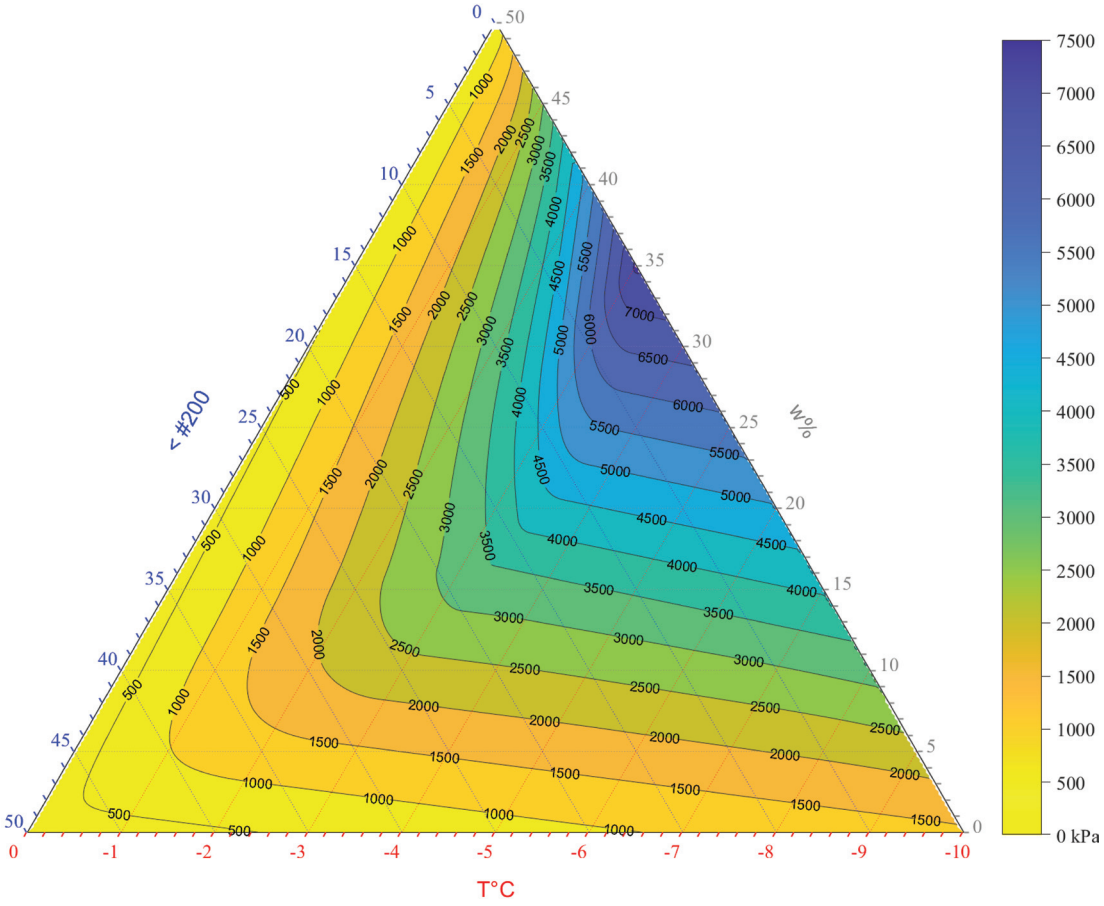


**Fig. 20** $P_{frost}$ estimation of fine grains and water content

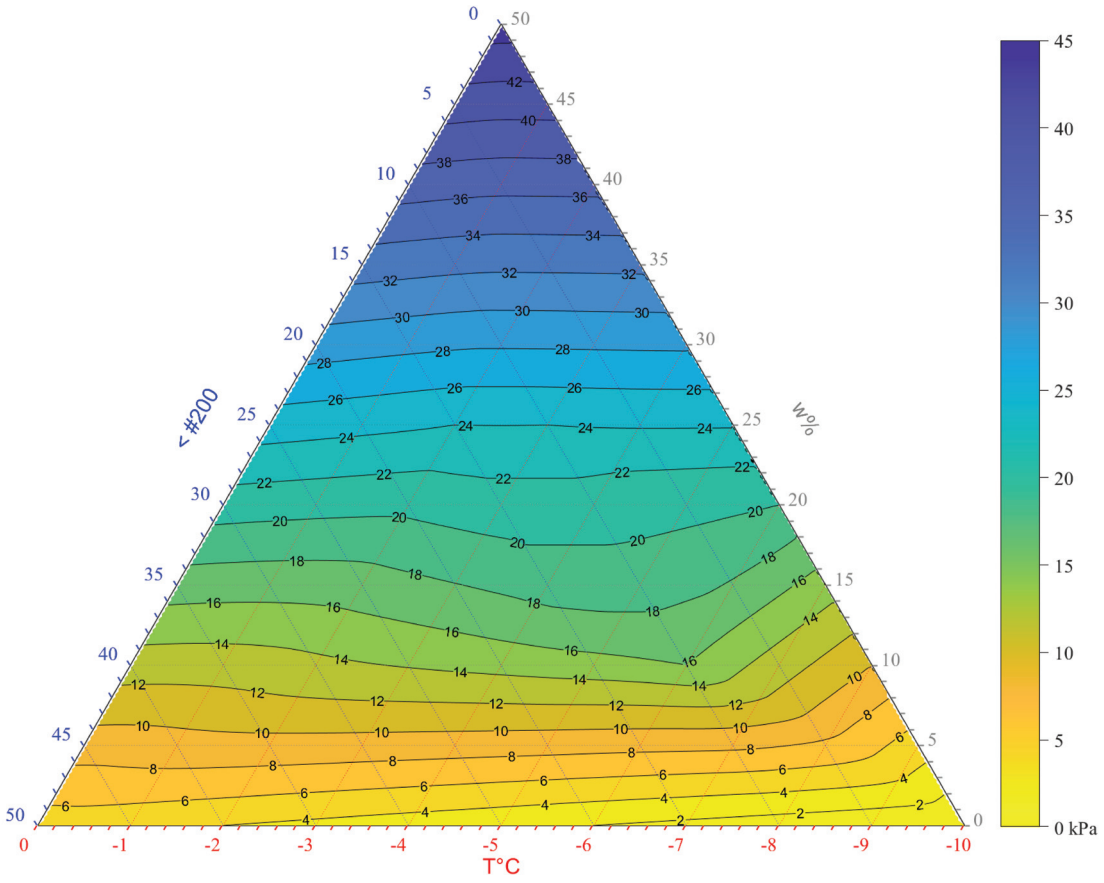


**Fig. 21** $P_{heave}$ prediction based on fine grains and water content

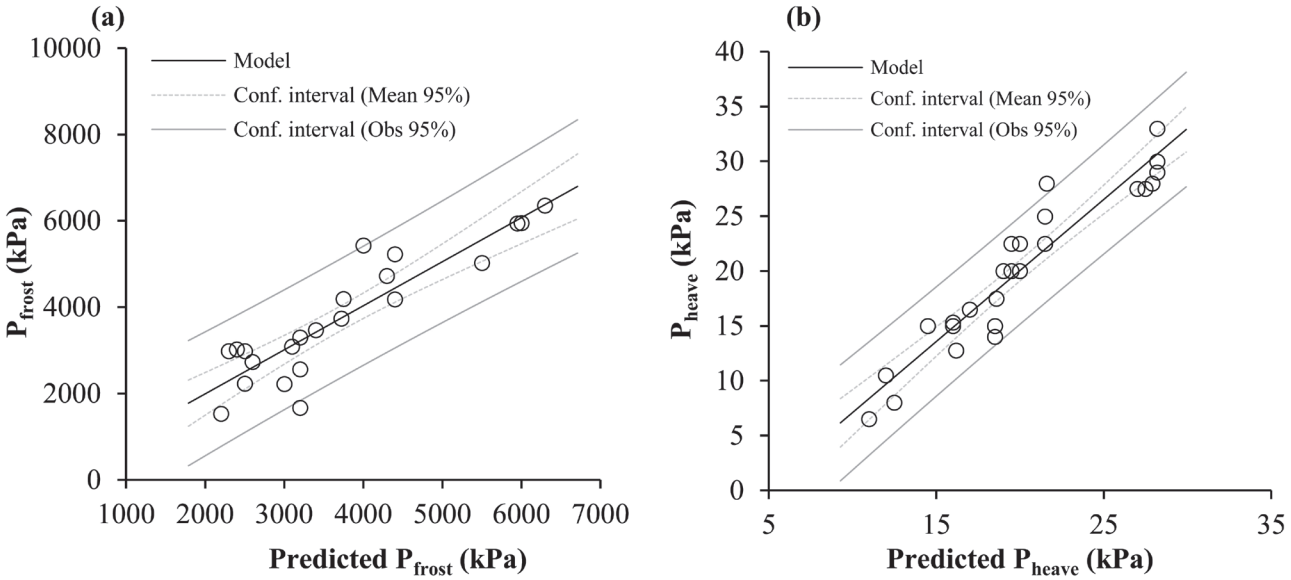


**Fig. 22** Relationships between the experimental test dataset and the values predicted by the chart: $P_{frost}$ (a) and $P_{heave}$ (b)

**Table 12** Goodness-of-fit of the ternary diagram

| Independent variable | Dependent variable | AIC | RMSE | $R^2$ |
|---|---|---|---|---|
| T, w%, >#200 | $P_{frost}$ | 286.63 | 646.12 | 0.81 |
| T, w%, >#200 | $P_{heave}$ | 45.85 | 2.327 | 0.90 |

## CONCLUSIONS

A device was developed to model the mechanical behaviour of soil samples at different temperatures (0°C and below), and experiments were performed using this device. These observations are discussed below:

1) The soils in the four mountainous areas were classified, and it was determined that the soil classes ranged from ML to GW and were generally classified as GM and SM at all locations. The percentage of fine grains in the soil samples decreased with increasing altitude, whereas that of coarse grains increased.
2) The physical properties of soil cause different mechanical behaviours at various temperatures. The strength of the frozen soil effectively increases if it includes a high percentage of fine particles. For example, the fine-grain soil strength (7274.5 kPa) was higher than the others. However, the plasticity index and water content significantly affected frost strength. The strength of the specimens with excess water content changed visibly with decreasing temperature. Water in the grains exhibited binding characteristics in the structure at temperatures below zero, which is another factor that causes increased strength.
3) High heaving pressure values (43.97 kPa) were observed in the fine-grained soil samples. In addition, samples with a high water content exhibited higher swelling pressures at low temperatures.
4) Ternary diagrams are developed based on the predicted temperature, water content, fine-grained ratio, soil strength, and swelling pressure. The frost strength and heaving pressure could be estimated with high $R^2$ values ($R^2$: 0.81 for strength, $R^2$: 0.90 for swelling pressure). These charts can assess the strength and heaving of the railway base materials at low temperatures.

## ACKNOWLEDGEMENTS

This study was funded by the Turkish National Scientific Committee, TUBITAK (Project No114Y088). The authors thank the editor and the reviewers for their helpful comments.

## REFERENCES

Addinsoft. 2024. *XLSTAT statistical and data analysis solution*. Long Island, NY. https://www.xlstat.com

Adeli Ghareh Viran, P., Binal, A. 2018. Effects of repeated freeze–thaw cycles on physico-mechanical properties of cohesive soils. *Arabian Journal of Geosciences 11,* Article No: 250. https://doi.org/10.1007/s12517-018-3592-5

Akçar, N., Yavuz, V., Ivy-Ochs, S., Kubik, P.W., Vardar, M., Schlüchter, C. 2007. Paleoglacial records from Kavron Valley, NE Turkey: Field and cosmogenic exposure dating evidence. *Quaternary International 164–165*, 170–183. https://doi.org/10.1016/j.quaint.2006.12.020

Binal, A., Binal, B.E. 2020. Ternary Diagrams for Predicting Strength of Soil Ameliorated with Different Types of Fly Ash. *Arabian Journal for Science and Engineering 45*, 8199–8217. https://doi.org/10.1007/s13369-020-04669-2

Brandl, H. 2008. Freezing-thawing behaviour of soils and unbound road layers. *Slovak Journal of Civil Engineering 3*, 4–12.

Dede, V., Dengiz, O., Zorlu, B.Ş., Zorlu, K. 2021. The effect of temperature change due to elevation on soil properties in periglacial landforms in Ilgaz Mountains. *Turkish Geographical Review 78*, 23–32. https://doi.org/10.17211/tcd.1002568

Dede, V., Turan, İ.D., Dengiz, O., Serin, S., Pacci, S. 2022. Effects of Periglacial Landforms on Soil Erosion Sensitivity Factors and Predicted by Artificial Intelligence Approach in Mount Cin, NE Turkey. *Eurasian Soil Science 55*, 1857–1870. https://doi.org/10.1134/S106422932260138X

Dore, G., Zubeck, H.K. 2009. *Cold Regions Pavement Engineering*. ASCE Press, McGraw-Hill.

Erinç, S. 1953. *Geography of Eastern Anatolia*. Istanbul: Sucuoglu Publ.

Haykin, S. 1994. *Neural Networks: A Comprehensive Foundation*. Upper Saddle River: Prentice Hall PTR.

Hermansson, Å., Spencer Guthrie, W. 2005. Frost heave and water uptake rates in silty soil subject to variable water table height during freezing. *Cold Regions Science and Technology 43*, 128–139. https://doi.org/10.1016/j.coldregions.2005.03.003

Ho, R. 2006. *Handbook of Univariate and Multivariate Data Analysis and Interpretation with SPSS*. https://doi.org/10.1201/9781420011111

Huixin, Z., Zhiqin, W., Zhaoyu, L. 2012. Experimental Study on Frost heave of Silty Clay in Seasonally Frost Soil Regions. *Procedia Engineering 28*, 282–286. https://doi.org/10.1016/j.proeng.2012.01.720

ISSMFE Technical Committee TC-8: FROST. *Frost in Geotechnical Engineering: International Symposium Saariselkä, Finland, 13–15 March, 1989*. Vol. 2.

Jing, X., Cui, Z., Doh, S., Ma, L., Wei, L., Liu, D. 2021. Effect of freeze-thaw cycles on shear strength of unsaturated bentonite modified clay. *Physics and Chemistry of the Earth, Parts A/B/C121*, Article No: 102955. https://doi.org/10.1016/j.pce.2020.102955

Karamut, R.O. 2016. *The Investigation of Strength and Deformability of Soil at Low Temperatures*. Msc. Thesis, Hacettepe University. [In Turkish].

Konrad, J.-M. 1999. Frost susceptibility related to soil index properties. *Canadian Geotechnical Journal 36*, 403–417. https://doi.org/10.1139/t99-008

Korkmaz, M., Binal, A., Kaya, H., Kırmacı, V. 2023. ANN based ternary diagrams for thermal performance of a Ranque Hilsch vortex tube with different working fluids. *Thermal Science and Engineering Progress 40*, Article No: 101803. https://doi.org/10.1016/j.tsep.2023.101803

Li, Y., Wang, Z., Luo, Y. 2021. Physical and Mechanical Characteristics of Shallow Expansive Soil due to Freeze-Thaw Effect with Water Supplement. *Advances in Civil Engineering 2021*, Article No: 6615049. https://doi.org/10.1155/2021/6615049

Liu, Y., Wang, Q., *et al.* 2019a. Experimental investigation of the geotechnical properties and microstructure of lime-stabilized saline soils under freeze-thaw cycling. *Cold Regions Science and Technology 161*, 32–42. https://doi.org/10.1016/j.coldregions.2019.03.003

Liu, Y., Deng, H., Xu, J., Tian, G., Deng, J. 2022. Association Study on the Pore Structure and Mechanical Characteristics of Coarse-Grained Soil under Freeze-Thaw Cycles. *Minerals 12*. https://doi.org/10.3390/min12030314

Liu, Z., Liu, J., Li, X., Fang, J. 2019b. Experimental study on the volume and strength change of an unsaturated silty clay upon freezing. *Cold Regions Science and Technology 157*, 1–12. https://doi.org/10.1016/j.coldregions.2018.09.008

Llears, C. 2005. Path Analysis. *In*: Kimberly Kempf-Leonard (ed.) *Encyclopedia of Social Measurement*, 25–30.

Loranger, B., Doré, G., Hoff, I., Scibilia, E. 2022. Assessing soil index parameters to determine the frost susceptibility of crushed rock aggregates. *Cold Regions Science and Technology 197*, Article No: 103489. https://doi.org/10.1016/j.coldregions.2022.103489

Ott, R.L., Longnecker, M. 2001. *Inferences about More than Two Population Central Values. An Introduction to Statistical Method and Data Analysis*, Fifth Edition. Duxbury, USA: Thomson Learning, 1213 pp.

Oztas, T., Fayetorbay, F. 2003. Effect of freezing and thawing processes on soil aggregate stability. *CATENA5 2*, 1–8. https://doi.org/10.1016/S0341-8162(02)00177-7

Polat, S. 2003. *Hydrogeomorphology study of Karasu River basin*. Msc Thesis, Marmara University Institute of Social Sciences. [In Turkish].

Qi, J., Hu, W., Ma, W. 2010. Experimental study of a pseudo-preconsolidation pressure in frozen soils. *Cold Regions Science and Technology 60*, 230–233. https://doi.org/10.1016/ j.coldregions.2009.10.008

Rene, E.R., Veiga, M.C., Kennes, C. 2009. Experimental and neural model analysis of styrene removal from polluted air in a biofilter. *Journal of Chemical Technology & Biotechnology 84*, 941–948. https://doi.org/10.1002/jctb.2130

Rumelhart, D.E., Hinton, G.E., Williams, R.J. 1986. Learning representations by back-propagating errors. *Nature 323*, 533–536. https://doi.org/10.1038/323533a0

Sarıkaya, M.A., Çiner A., Zreda M. 2003. Late Quaternary glacial deposits of the Erciyes Volcano. *Bulletin of Earth Sciences 27*, 59–74. Hacettepe University.

Slunga, E., Saarelainen, S. 2005. Determination of frost-susceptibility of soils. *In*: *Proceedings of the 16th International Conference on Soil Mechanics and Geotechnical Engineering*, 3577–3578.

Sun, Y., Meng, S., Wang, M., Mu, H., Tang, X. 2021. Deterioration effect of freeze-thaw on mechanical properties of roadbed clay under un-

favourable conditions. *Bulletin of Engineering Geology and the Environment 80*, 4773–4790. https://doi.org/10.1007/s10064-021-02203-8

Wang, D., Ma, W., Niu, Y., Chang, X., Wen, Z. 2007. Effects of cyclic freezing and thawing on mechanical properties of Qinghai–Tibet clay. *Cold Regions Science and Technology 48*, 34–43. https://doi.org/10.1016/j.coldregions.2006.09.008

Wang, J., Wang, Q., Lin, S., Han, Y., Cheng, S., Wang, N. 2020. Relationship between the Shear Strength and Microscopic Pore Parameters of Saline Soil with Different Freeze-Thaw Cycles and Salinities. *Symmetry 12*, 1709. https://doi.org/10.3390/sym12101709

Wang, T., Ma, H., Liu, J., Luo, Q., Wang, Q., Zhan, Y. 2021. Assessing frost heave susceptibility of gravelly soils based on multivariate adaptive regression splines model. *Cold Regions Science and Technology 181*, Article No: 103182. https://doi.org/10.1016/j.coldregions.2020.103182

Zhu, Y.L. 1988. Studies on strength and creep behaviour of frozen soils in China. *Journal of glaciology and geocryology 10*, 332–337.